PHYSICAL REVIEW B VOLUME 6, NUMBER 10 15 NOVEMBER 1972

Raman Scattering and Far-Infrared Absorption Induced by Silver Ions in Sodium Chloride*

G. P. Montgomery, Jr.† and Miles V. Klein
Department of Physics and Materials Research Laboratory, University of Illinois, Urbana, Illinois 61801

and

B. N. Ganguly‡ and R. F. Wood
Solid State Division, Oak Ridge National Laboratory, Oak Ridge, Tennessee 37830

(Received 19 June 1972)

A detailed experimental and theoretical study of the defect-induced far-infrared and first-order-Raman spectra of the NaCl : Ag^+ system has been made. New low-temperature Raman data revealed many singularities pertaining to pure and perturbed phonons. Only a few of the singularities could be assigned to particular phonon critical points. The theoretical calculations were based on the so-called "lattice-relaxation" model, neutron-determined phonon parameters, and an accurate Brillouin-zone interpolation scheme. The calculated unperturbed T_{2g} Raman spectrum fit the data well. The unperturbed E_g spectrum gave a poor fit, primarily because it did not explain a very strong experimental E_g peak at 96 cm^{-1}. This peak could be explained as an incipient resonance mode caused by relatively large decreases in the central-force constants. The infrared spectrum was fit well by assuming somewhat smaller central-force-constant decreases. The A_{1g} Raman spectrum could not be fit using force-constant decreases; it required an increase of the nearest-neighbor central-force constant. These results could be understood semiquantitatively as due to symmetry-dependent Coulomb contributions to force-constant changes resulting from lattice relaxation. The absolute scattering efficiencies and cross sections were determined for the three Raman symmetries and had T_{2g}: A_{1g}: E_g intensity ratios of approximately 4 : 10 : 20.

I. INTRODUCTION

Three experimental techniques for studying perturbed lattice vibrations are the measurement of thermal conductivity, far-infrared (ir) absorption, and first-order-Raman scattering. Thermal-conductivity measurements provide information about an integral over perturbed phonon properties; ir and Raman measurements provide direct information about the density of states associated with certain combinations of atomic displacements in the perturbed crystal.

This paper describes an experimental and theoretical study of defect-induced far-ir and first-order-Raman spectra of the NaCl : Ag^+ system. We present here the results of detailed Raman scattering at room temperature, 78 and 7 K. The low-temperature spectra are new and add considerably to previously published room-temperature data from Kaiser and co-workers.[1-3] The theoretical calculations are intended to provide a consistent interpretation of the Raman data and of previous experimental ir results.[4] They make use of neutron-determined phonon parameters and an interpolation scheme to yield accurate computed spectra that contain many fine details. The need for these new computations is readily apparent from the following brief review of the published experimental and theoretical work on the vibrational properties of the NaCl : Ag^+ system.

Caldwell and Klein (CK) observed that the thermal conductivity of NaCl crystals doped with Ag^+ exhibits a depression near 40 K.[5] They attributed this "dip" to phonon scattering from a 53-cm^{-1} resonance mode previously observed in the ir by Weber.[6] CK used a "preneutron" shell model and calculated eigenvalues and eigenvectors for the NaCl-host-crystal phonons at 64 000 points in the Brillouin zone. These were then used to calculate appropriate perturbed Green's functions. The perturbation was characterized by a mass change at the defect site and a change in the central-force constant between the impurity and its six-nearest-neighbor Cl^- ions. The thermal-conductivity data were reasonably well explained by this model if the central-force constant between the impurity and its nearest neighbors was decreased by about 60% of its host-crystal value.

Subsequently Macdonald, Klein, and Martin (MKM)[4] carried out an experimental and theoretical study of the far-ir-absorption spectra of NaCl doped with various impurities, including Ag^+. They found that the central-force-constant-change model used by CK could explain neither the strength of the 53-cm^{-1} resonance mode nor the additional defect-induced one-phonon absorption peaks observed above 100 cm^{-1}. Over-all agreement with experiment was improved considerably by use of a model in which the noncentral-force constant between the impurity and its nearest neighbors was decreased by 10–15% and the central-force constant slightly increased. We now

feel that the apparent failure of the central-force-constant model found by MKM was an artifact due primarily to the use of inaccurate "preneutron"-shell-model parameters.

Kaiser and co-workers[1-3] observed a strong 85-cm^{-1} E_g Raman peak at room temperature in NaCl : Ag^+ as well as several peaks at higher frequencies, the most prominent being a T_{2g} peak at 171 cm^{-1}. They interpreted their data with the help of some calculations of Benedek and Nardelli (BN), [7] who used the deformation-dipole model to calculate host-phonon frequencies and eigenvectors at 4096 points in the Brillouin zone. The BN calculation predicted correctly the 53-cm^{-1} ir resonance and the 85-cm^{-1} E_g Raman resonance for a 50% decrease in the nearest-neighbor central-force constant. These calculations did not adequately describe the strong high-frequency T_{2g} peak or the high-frequency ir structure. Finally both the CK and BN calculations fail to account for the finer details of the low-temperature Raman spectra to be presented here.

It is apparent, then, that no single defect model has been able to explain the known experimental results on NaCl : Ag^+. The force-constant changes that have been used to fit a given set of data seem to vary strongly with the model used to calculate the host-crystal phonons. Since both CK and BN calculations were done before the phonon-dispersion curves for NaCl were experimentally determined, it was difficult to decide whether some of the discrepancies were due to inadequacies in the force-constant models used for the impurity or in the model host-crystal phonons. Low-temperature neutron scattering data are now available for NaCl. [8] This enables us to obtain a better shell model for the host-crystal phonons from a fit to the neutron results. [9] One purpose of this paper is to show that if this realistic phonon model is used with a more elaborate defect model and a more accurate computational procedure, one can obtain considerably better agreement with both the ir and Raman spectra for NaCl : Ag^+.

The remainder of this paper is planned as follows: In Sec. II we describe briefly the theories underlying the ir absorption and Raman scattering for a defect system. Section III describes techniques and results of the experiments. Section IV treats some of the calculational procedures, and Sec. V then presents and discusses the results of the calculations.

II. THEORETICAL CONSIDERATIONS

The theory of impurity-induced infrared absorption and first-order-Raman scattering in alkali halides has been described by several authors.[10-13] We shall now summarize the principal results of their work.

The first-order-ir absorption by lattice vibrations in an undoped polar diatomic cubic crystal occurs as a single band at the $q=0$ transverse-optical-phonon frequency. When an impurity is present the "$q=0$ selection rule" is violated, and many other phonons contribute to the absorption. For a monovalent impurity in an alkali halide the impurity-induced absorption coefficient is[10]

$$\alpha(\omega)=\frac{-4\pi N_I}{n(\omega)c}\,\frac{\omega}{(\omega_{\mathrm{TO}}^2-\omega^2)^2}\,\frac{e^{*2}(n_\infty^2+2)^2}{9\mu v}\times\lim_{\epsilon\to 0^+}\mathrm{Im}\langle 0,\mathrm{TO}|\,t(\omega^2+i\epsilon)\,|0,\mathrm{TO}\rangle\ . \quad (2.1)$$

Here N_I is the defect concentration per unit volume, c the velocity of light, e^* the Szigeti effective charge, ω_{TO} the $q=0$ TO phonon frequency, μ the reduced ionic mass, and v the volume of a unit cell; $n_\infty=\epsilon_\infty^{1/2}$ is the high-frequency refractive index; $|0,\mathrm{TO}\rangle$ is the normalized eigenvector of the TO phonon at $q=0$; $t(\omega^2+i\epsilon)$ is the t matrix within the defect subspace; and $n(\omega)$ is the frequency-dependent refractive index given by

$$[n(\omega)]^2=\epsilon_\infty+\frac{\epsilon_0-\epsilon_\infty}{1-\omega^2/\omega_{\mathrm{TO}}^2} \quad (2.2)$$

ϵ_0 is the low-frequency dielectric constant. The t matrix in Eq. (2.1) can be expressed in terms of the defect matrix Δ and G^0, the unperturbed Green's-function matrix of the host lattice, via $t=(1+\Delta G^0)^{-1}\Delta$. The defect matrix Δ has the full symmetry of the O_h point group of the impurity. Both Δ and the t matrix may be block diagonalized into components belonging to the irreducible representations of the O_h group. Only the T_{1u} block of the t matrix will couple to the vector $|0,\mathrm{TO}\rangle$ eigenstates.

Raman-scattering results from vibration-induced changes in the electronic polarizability of a system. In a perfect alkali halide crystal every ion is at a site of inversion symmetry. Consequently, all first-order polarizability derivatives are identically zero, and there is no first-order-Raman effect. When an impurity is substituted at a lattice site, the inversion symmetry is destroyed at the neighboring sites, and certain atomic displacements of the neighbor atoms have nonzero first-order polarizability derivatives. The impurity also represents a departure from translational symmetry. This implies that atomic displacements responsible for Raman scattering need not correspond to $q=0$ optic phonons. The first-order-Raman spectrum in a perturbed crystal is a continuum reflecting the density of states for those atomic displacements rendered Raman active by the presence of the impurity. It can be observed even if the interatomic force constants in the vicinity of the defect are unchanged from those of the perfect crystal. Generally the force constants are some-

TABLE I. Raman tensors for group O_h.

A_{1g}	E_g		T_{2g}		
$\begin{pmatrix} a & 0 & 0 \\ 0 & a & 0 \\ 0 & 0 & a \end{pmatrix}$	$\frac{1}{2}\begin{pmatrix} b & 0 & 0 \\ 0 & b & 0 \\ 0 & 0 & -2b \end{pmatrix}$	$\frac{\sqrt{3}}{2}\begin{pmatrix} b & 0 & 0 \\ 0 & -b & 0 \\ 0 & 0 & 0 \end{pmatrix}$	$\begin{pmatrix} 0 & c & 0 \\ c & 0 & 0 \\ 0 & 0 & 0 \end{pmatrix}$	$\begin{pmatrix} 0 & 0 & 0 \\ 0 & 0 & c \\ 0 & c & 0 \end{pmatrix}$	$\begin{pmatrix} 0 & 0 & c \\ 0 & 0 & 0 \\ c & 0 & 0 \end{pmatrix}$

what altered, sometimes enough to produce localized and/or resonance modes.

In NaCl: Ag^+ with its O_h impurity-site symmetry, the Raman-active modes must have A_{1g}, E_g, or T_{2g} symmetry. It is reasonable to assume that in the doped crystal the polarizability derivatives will be nonzero only in the neighborhood of the impurity. It is then convenient to discuss impurity-induced Raman scattering in terms of irreducible configurations or coordinates $X_n(\Gamma j)$. These are symmetry-adapted linear combinations of displacements of the nth shell of atoms around the impurity with the transformation properties of the jth row of the Γth irreducible representation of the impurity-site point group. Actual calculations are done with mass-reduced coordinates $Q_n(\Gamma j) = M_n^{1/2}(\Gamma) X_n(\Gamma j)$, where $M_n(\Gamma)$ is the appropriate reduced mass.

The differential Stokes–Raman-scattering cross section for photons per unit solid angle per unit frequency range at frequency shift ω may be written as[14]

$$\frac{d^2\sigma}{d\omega\, d\Omega} = \frac{\omega_L \omega_S^3 \hbar}{c^4} [1 + n_0(\omega)] \sum_{\Gamma, j, n, m} \left(\hat{\eta}_S \cdot \frac{\partial \overleftrightarrow{\alpha}}{\partial Q_n(\Gamma j)} \cdot \hat{\eta}_L \right) \times \left(\hat{\eta}_S \cdot \frac{\partial \overleftrightarrow{\alpha}}{\partial Q_m(\Gamma j)} \cdot \hat{\eta}_L \right) \frac{\rho_{nm}(\omega, \Gamma)}{2\omega} . \quad (2.3)$$

Here $\hat{\eta}_L$ and $\hat{\eta}_S$ are, respectively, unit vectors along the directions of polarization of the incident laser radiation of frequency ω_L and the scattered Raman radiation of frequency $\omega_S = \omega_L - \omega$; $[\partial \overleftrightarrow{\alpha} / \partial Q_n(\Gamma j)]$ is the polarizability derivative induced by the impurity; and $n_0(\omega) = (e^{\hbar\omega/k_B T} - 1)^{-1}$. The quantity $\rho_{nn}(\omega, \Gamma)$ is the perturbed normalized projected density of states for shell n, and for $n \neq m$, $\rho_{nm}(\omega, \Gamma)$ is a cross term describing intershell coupling:

$$\rho_{nm}(\omega, \Gamma) = \frac{2\omega}{\pi} \lim_{\epsilon \to 0^+} \operatorname{Im} \langle Q_n(\Gamma j) | G(\omega^2 + i\epsilon) | Q_m(\Gamma j) \rangle \equiv \frac{2\omega}{\pi} \operatorname{Im} G_{nm}(\omega^2, \Gamma) . \quad (2.4)$$

In Eq. (2.4) G is the perturbed Green's-function matrix. It has the symmetry of the O_h point group and hence is block diagonalized by the transformation to the coordinates $Q_n(\Gamma j)$. For a given block, i.e., given (Γj), only the shell indices n, m remain. In Sec. IV we shall say more about the matrices $G_{nm}(\omega^2, \Gamma)$.

Two additional assumptions will be made: One is that the $\partial\alpha/\partial Q$'s are independent of ω; this is consistent with the adiabatic theorem usually invoked to derive an equation such as Eq. (2.3). The other assumption is that only the first shell of neighbors has nonzero $\partial\alpha/\partial Q$'s. Then Eq. (2.3) becomes

$$\frac{d^2\sigma}{d\omega\, d\Omega} = \frac{\omega_L \omega_S^3 \hbar}{c^4} [(1 + n_0(\omega)] \times \sum_{\Gamma, j} \left| \hat{\eta}_S \cdot \frac{\partial \overleftrightarrow{\alpha}}{Q_1(\Gamma j)} \cdot \hat{\eta}_L \right|^2 \frac{\rho_{11}(\omega, \Gamma)}{2\omega} . \quad (2.5)$$

By proper choice of the unit vectors $\hat{\eta}$ one can, in effect, observe just a single term from the sum over Γ. It will then have the low-temperature frequency dependence of the factor $\rho_{11}(\omega, \Gamma)/\omega$. Thus the defect-induced first-order-Raman scattering is a direct measure of the perturbed density of states for those coordinates Q that have nonzero polarizability derivatives.[11] The perturbed density of states thus obtained will exhibit peaks at the frequencies of localized or resonance modes, if any, and will also manifest the critical points or Van Hove singularities associated with pure-crystal phonon spectra.

The forms of the polarizability-derivative tensor $\partial\alpha/\partial Q$ are determined by symmetry considerations.[15] The Raman tensors for the relevant O_h group are given in Table I. The experimental geometry of a Raman experiment is denoted by the symbol $\hat{k}_L(\hat{\eta}_L \hat{\eta}_S)\hat{k}_S$, where $\hat{k}_L$ and $\hat{k}_S$ denote the propagation directions of the incident and scattered light. Table II gives the Raman cross sec-

TABLE II. Raman cross sections for scattering geometries of this investigation.

$\hat{k}_L(\hat{\eta}_L\hat{\eta}_S)\hat{k}_S$	$\frac{d\sigma^2}{d\omega d\Omega}$
(100) Geometry: $X = (100)$, $Y = (010)$, $Z = (001)$	
$Z(XX)Y$	$a^2 W(A_{1g}) + b^2 W(E_g)$
$Z(XZ)Y$	$c^2 W(T_{2g})$
$Z(YX)Y$	$c^2 W(T_{2g})$
$Z(YZ)Y$	$c^2 W(T_{2g})$
(110) Geometry: $X = (1/\sqrt{2})(110)$, $Y = (1/\sqrt{2})(\bar{1}10)$, $Z = (001)$	
$Z(XX)Y$	$a^2 W(A_{1g}) + \frac{1}{4} b^2 W(E_g) + c^2 W(T_{2g})$
$Z(XZ)Y$	$c^2 W(T_{2g})$
$Z(YX)Y$	$\frac{3}{4} b^2 W(E_g)$
$Z(YZ)Y$	$c^2 W(T_{2g})$

TABLE III. Absolute Raman-scattering efficiencies and cross sections in NaCl: Ag^+ for 4880-Å exciting light.

	E_g	T_{2g}	A_{1g}
$dR/d\Omega$ (cm sr)$^{-1}$	2.06×10^{-9}	4.41×10^{-10}	1.13×10^{-9}
$d\sigma/d\Omega$ (cm^2/sr)	1.88×10^{-29}	4.00×10^{-30}	1.03×10^{-29}

tions to be expected from the different scattering geometries used in this investigation. The quantities $W(\Gamma)$ used in the table are defined by

$$W(\Gamma)=\frac{\omega_L\omega_S^3\hbar[(1+n_0(\omega)]\rho_{11}(\omega,\Gamma)}{2\omega c^4}\ . \qquad (2.6)$$

Note that the (100) geometry does not allow unambiguous separation of A_{1g} and E_g spectra, whereas the (110) geometry enables the E_g spectrum to be observed by itself, so that the A_{1g} spectrum can be obtained by a weighted subtraction procedure.

III. EXPERIMENTAL

A. Technique

NaCl : Ag^+ samples used in this investigation were taken from the boules grown by CK[5] for thermal-conductivity measurements and subsequently used by MKM[16,4] for ir-absorption measurements. The uv-absorption techniques used to determine the impurity concentration have been described previously.[5] The Raman spectra shown in this paper were obtained using a crystal containing 0.5-mole% Ag^+, i.e., 1.1×10^{20} Ag^+ ions per cm^3. Measurements made on samples of lower concentrations demonstrated that all the strong features of the spectra presented here scale linearly with impurity concentration.

The Raman sample was mounted in a top-loading metal cryostat with antireflection-coated Pyrex windows. The sample chamber was isolated from the main vacuum region, and the sample was cooled by filling this chamber with helium exchange gas in thermal contact with a liquid-nitrogen or liquid-helium reservoir. Sample temperatures were measured with a gold + 0.07-at.%-Co vs copper thermocouple[17] attached to the sample block. The accuracy of our temperature measurements is ± 1 K.

The Raman spectra were taken in the (110) right-angle scattering geometry (Table II) using an argon-ion laser operating at 4880 Å with 1-W output, a Spex double monochromator, and a cooled ITT FW-130 photomultiplier tube with S-20 response and 2 dark counts/sec. The incident laser polarization was controlled with a half-wave plate, and a sheet of polarizing material was used for analysis of the scattered radiation. Since the spectrometer response may differ for light polarized parallel and perpendicular to the grating rulings, a polarization scrambler was placed between the polarizer and the monochromator entrance slit to ensure that the Raman radiation entered the spectrometer as unpolarized light. Photon-counting electronics were used to obtain the Raman spectra in digital form. The digital output was recorded on punched paper tape by a teletype and processed by computer. Data points were taken every 0.2 Å with 10-sec dwell time at each point. Each spectrum shown in this paper is the average of several such scans.

B. Results

The Raman spectra of NaCl : Ag^+ at 300, 78, and 7 K are shown in Figs. 1–4. In each figure the curves have been displaced vertically from one another for easier viewing. The vertical scales are different for each temperature as indicated in the figure captions in order that details of the lower-temperature spectra are not lost in comparison with the stronger room-temperature curves. The spectral slit width for these measurements was about 2.5 cm^{-1} for all the spectra. All the spectra in Figs. 1–4 have been normalized to the host-lattice two-phonon Raman spectrum by comparing the two-phonon scattering in the pure and

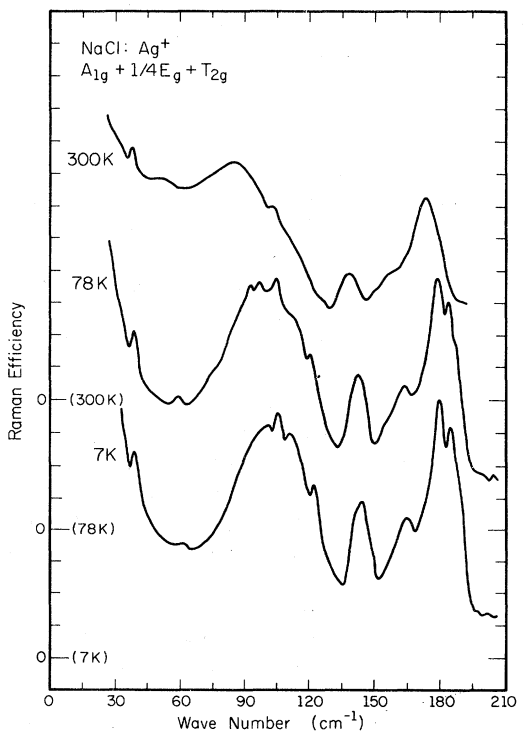

FIG. 1. The $(A_{1g}+\frac{1}{4}E_g+T_{2g})$ Raman spectrum of NaCl: Ag^+. Each vertical division represents 200 counts/sec at 300 K, 75 counts/sec at 78 K, and 50 counts/sec at 7 K. The curves have been shifted vertically for easier viewing, and the zero levels for each temperature are indicated.

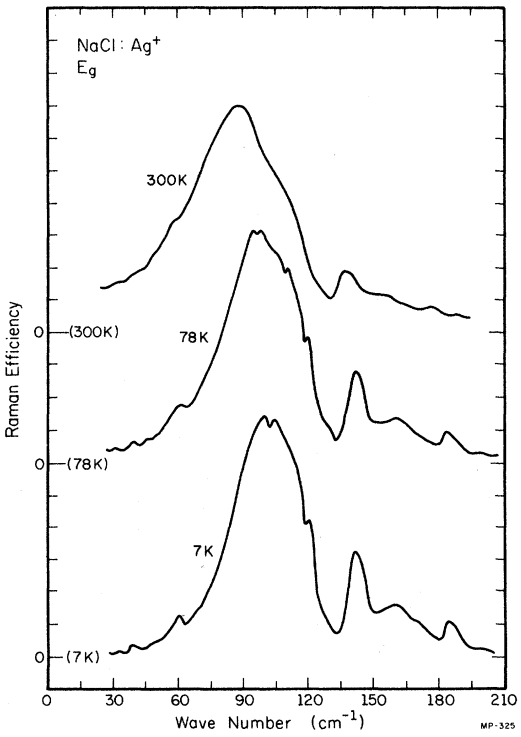

FIG. 2. The E_g Raman spectrum of NaCl:Ag^+. Each vertical division represents 400 counts/sec at 300 K, 200 counts/sec at 78 K, and 100 counts/sec at 7 K. The curves have been shifted vertically for easier viewing, and the zero levels for each temperature are indicated.

doped crystals.

The combined $(A_{1g}+\frac{1}{4}E_g+T_{2g})$ two-phonon spectrum of the host lattice is shown as a function of temperature in Fig. 5. Examination of Figs. 1–4 in the light of this figure shows that, at room temperature, the NaCl: Ag^+ spectra contain a small amount of residual host-crystal scattering near 30 cm^{-1} and above 150 cm^{-1}. This residual scattering is drastically reduced as the temperature is lowered. At 7 K the 30-cm^{-1} scattering has completely disappeared, and the scattering between 150 and 210 cm^{-1} has been reduced to a level below the base line at the high-frequency limit of the impurity-induced scattering. We have not attempted to subtract the residual two-phonon scattering from any of the curves in Figs. 1–4.

The room-temperature spectra are in good agreement with previously published results.[1-3] We observe a strong E_g peak in the 85–90-cm^{-1} region, which is due to a (near-) resonant mode involving motion of the neighbors of the Ag^+ impurity. This peak will be discussed in detail in subsequent sections. A strong T_{2g} scattering is observed between 150 and 190 cm^{-1}. The 135-cm^{-1} band has both E_g and T_{2g} components. Essentially no A_{1g} scattering is observed; the rise in the A_{1g} spectrum above 160 cm^{-1} is primarily due to the residual scattering from the host crystal.

As the sample is cooled, the E_g resonance peak shifts to higher frequencies and narrows, and additional structure is revealed in the E_g and T_{2g} spectra. Perhaps the most dramatic change is the appearance of relatively strong A_{1g} scattering above 130 cm^{-1}. At 300 K this scattering was obscured by the host-crystal two-phonon scattering, which has decrease to below 140 counts/sec at 7 K.

It should be noted that the A_{1g} spectrum has to be obtained by subtracting the T_{2g} scattering and $\frac{1}{4}$ of the E_g scattering from the $A_{1g}+\frac{1}{4}E_g+T_{2g}$ spectrum. In the T_{2g} and E_g spectra, which are taken with incident and scattered light having mutually perpendicular polarizations, the stray light is generally considerably lower than in the combined spectrum for which the incident laser light and scattered Raman light have the same polarization. The effects of stray light can strongly affect the A_{1g} spectrum via the subtraction process, as can a small error in measuring the strong E_g scattering. It is felt that the broad peak in the low-temperature A_{1g} spectrum between 75 and 120 cm^{-1} is probably due to a combination of stray light and E_g leakage.

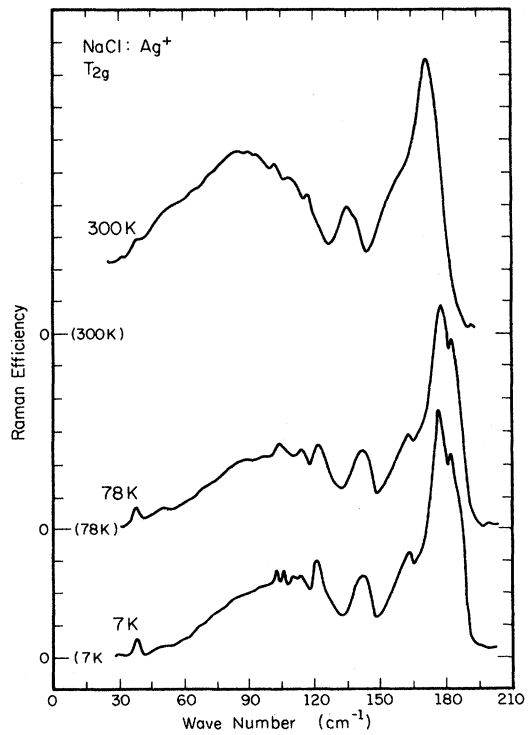

FIG. 3. The T_{2g} Raman spectrum of NaCl:Ag^+. Each vertical division represents 100 counts/sec at 300 K, 50 counts/sec at 78 K, and 25 counts/sec at 7 K. The curves have been shifted vertically for easier viewing, and the zero levels for each temperature are indicated.

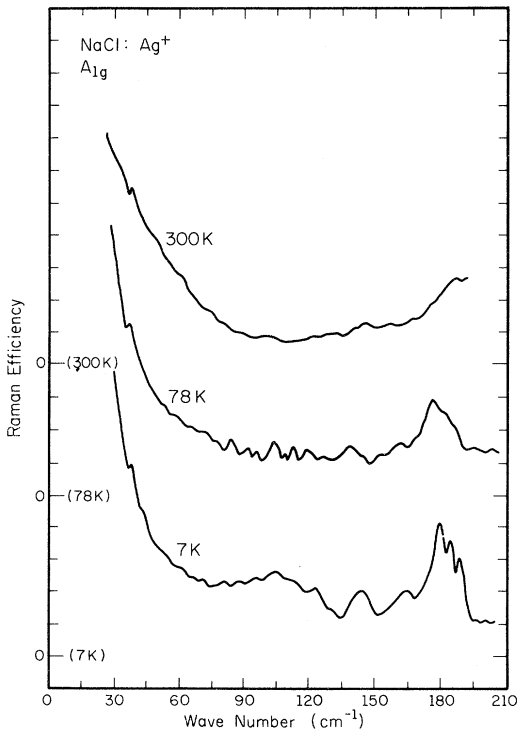

FIG. 4. The A_{1g} Raman spectrum of NaCl: Ag^+. Each vertical division represents 200 counts/sec at 300 K, 75 counts/sec at 78 K, and 50 counts/sec at 7 K. The curves have been shifted for easier viewing.

All scattering due to the presence of the Ag^+ is attributed to impurity-induced one-phonon scattering made possible by the breakdown of translational and inversion symmetry in the doped crystal. This scattering manifests the structure of the one-phonon density of states of the perturbed crystal. This is substantiated by the calculations to be described in the following sections.

We have put the host-crystal and impurity-induced scattering on an absolute basis by comparison with Raman scattering from the 992-cm^{-1} line of benzene, for which the absolute scattering cross section has been determined.[18,19] A detailed description of the measurements and of the considerations involved in comparing a continuum with a line spectrum are given elsewhere.[20] We find that 1 count/sec in Figs. 1–5 corresponds to a differential Raman efficiency $d^2R/d\omega\, d\Omega$ of 5.2×10^{-14} $(\text{cm sr cm}^{-1})^{-1}$, and in Figs. 1–4, 1 count/sec corresponds to a differential cross section $d^2\sigma/d\omega d\Omega$ of 4.74×10^{-34} $\text{cm}^2/\text{sr cm}^{-1}$. At 7 K, where low-frequency residual host-crystal scattering is negligible, we have also computed the frequency integrated efficiencies and cross sections. These are given in Table III. The E_g and T_{2g} cross sections should be accurate to about 15%. The probable stray light and E_g leakage makes the A_{1g} integrated cross section accurate to only about 50%. Note that the $T_{2g}:A_{1g}:E_g$ intensity ratios are about 4 : 10 : 20.

IV. CALCULATIONS

A. Defect Matrix and Green's Functions

The success of the "relaxation model" of Gethins, Timusk, and Woll[21] for ir sideband calculations of the H^- ion in alkali halides (U center) prompted us to employ the same model for Raman scattering and for ir-absorption calculations. This model assumes that the introduction of the defect produces a relaxation of A_{1g} symmetry, inward or outward depending on the nature of the defect, as well as a force-constant change between the defect and its first-nearest neighbors (1nn's). As a result of the 1nn displacements, a force-constant change between 1nn's and fourth-nearest neighbors (4nn's) also occurs. A calculation from first principles[22] for the U centers shows that a few percent change in the defect-1nn distance significantly alters the force constants between 1nn and 4nn ions. We note that, because of inversion symmetry about the defect site, the Raman-active vibrations involve the motion of the impurity's neighbors, the impurity itself remaining at rest. We might expect that the vibrational properties of

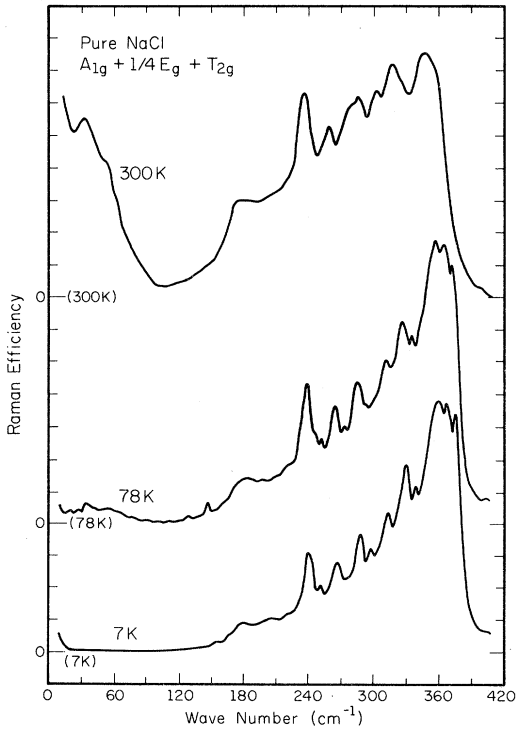

FIG. 5. The $(A_{1g}+\frac{1}{4}E_g+T_{2g})$ two-phonon Raman spectrum of pure NaCl. Each vertical division represents 125 counts/sec at 300 K, 60 counts/sec at 78 K, and 40 counts/sec at 7 K.

the nearest neighbors, which we have assumed to have the only nonzero $\partial\alpha/\partial Q$'s, would be quite sensitive to the particular set of force-constant changes involved in this model.

The defect subspace in this model contains the Cartesian displacements of the defect ion, the six 1nn ions, and six 4nn ions; its dimension is 39. The far-ir absorption and Raman scattering involve sets of linear combinations of defect space displacements which transform according to the T_{1u} and A_{1g}, E_g, T_{2g} representations for the O_h group, respectively. The set of symmetrized coordinates $Q_n(\Gamma j)$ of the defect space in the relaxation model is given in Ref. 22. The potential energy of the defect system can be expanded in terms of the complete set of symmetry coordinates as

$$U = U_0 + \tfrac{1}{2}\sum_{n\,m}\sum_{\Gamma j} K_{nm}(\Gamma j)\, Q_n(\Gamma j)\, Q_m(\Gamma j)\ , \qquad (4.1)$$

where

$$K_{nm}(\Gamma j) = \left(\frac{\partial^2 U}{\partial Q_n(\Gamma j)\,\partial Q_m(\Gamma j)}\right)_0 \ . \qquad (4.2)$$

n and m run over the shells of equivalent ions in the crystal. Γ runs over the irreducible representations of the point group, and j labels the orthogonal components of each Γ. The defect matrix is defined by

$$\Delta_{nm}(\Gamma j) = [K_{nm}(\Gamma j) - K^0_{nm}(\Gamma j)]\ , \qquad (4.3)$$

where the superscript 0 denotes the force constants of the perfect crystal and $K_{nm}(\Gamma j)$ are the force constants when the defect is present. For T_{1u} modes, there is an additional component of the defect matrix due to the mass change at the impurity site.

With ΔF_1, ΔF_4 ($\Delta F_1'$, $\Delta F_4'$) denoting the effective central- (noncentral-) force-constant changes between the defect and 1 nn ions and between 1 nn and 4 nn ions, respectively, the explicit expressions for the defect matrices for different irreducible representations are given below. We have set $n=0$ for the defect site, $n=1$ for 1nn ions, and $n=2$ for 4nn ions. For the T_{1u} mode we obtain

$$\Delta_{00} = (M_0 - M_d)\, M_0^{-1}\omega^2 + 2\Delta F_1/1.66M_0\ , \qquad (4.4a)$$

$$\Delta_{11} = (\Delta F_1 + \Delta F_4)/1.66M_1\ , \qquad (4.4b)$$

$$\Delta_{22} = \Delta F_4/1.66M_0\ , \qquad (4.4c)$$

$$\Delta_{01} = \Delta_{10} = -\sqrt{2}\Delta F_1/1.66(M_0 M_1)^{1/2}\ , \qquad (4.4d)$$

$$\Delta_{12} = \Delta_{21} = -\Delta F_4/1.66(M_0 M_1)^{1/2}\ , \qquad (4.4e)$$

$$\Delta_{02} = \Delta_{20} = 0\ . \qquad (4.4f)$$

In the above M_d is the mass of the defect, M_1 is the mass of a Cl^- ion, and $M_0 = M_2$ is the mass of the host Na^+ atom at the defect site. For the A_{1g} and E_g modes the matrix elements of Δ involving the central site do not appear, and Δ_{11}, Δ_{22}, and Δ_{12} have exactly the same form as above. The expressions for the T_{2g} mode are the same as those for A_{1g} and E_g but with the central-force constants replaced by noncentral-force constants. The units of the defect matrices are 10^{24} (rad/sec)^2, ΔF's are in dyn/cm, and masses are in amu. The appearance of the number 1.66 in Eqs. (4.4) results from a rounding off of the value of 1 amu, which equals 1.66042×10^{-24} g ($\frac{1}{12}$ of C^{12} mass).

The parameters ΔF_1, ΔF_4, $\Delta F_1'$, and $\Delta F_4'$ used above may be assumed to be dependent on symmetry. This explains why we call the ΔF's "effective" force-constant changes and can be understood as follows. Let us define "bare" force constants in terms of the appropriate derivatives of the potential energy with respect to individual ionic displacements. Suppose we change both the bare central-force constant f_1 between the impurity and its nearest neighbors and the bare central-force constants f_2 and f_3 acting among the various nearest neighbors themselves. We would then find different effective values of ΔF_1 for A_{1g}, T_{1u}, and E_g representations due to the combined effects of nonzero values of Δf_2 and Δf_3 and differences in displacement patterns of the nearest neighbors in the three different representations.

The imaginary parts of the unperturbed Green's-function matrices can be written in the Q representation as

$$\mathrm{Im}G^0_{nm}(\omega^2,\Gamma) = \pi\sum_{q,\lambda}\langle Q_n(\Gamma j)|\, v(q,\lambda)\rangle \times\langle v(q,\lambda)|\, Q_m(\Gamma j)\rangle\,\delta[\omega^2-\omega^2(q,\lambda)]\ . \qquad (4.5)$$

Here $v(q,\lambda)$ is the phonon eigenvector of the perfect crystal with wave vector $\vec{q}$ and polarization λ. It has components in real space given by

$$v_{\alpha\kappa l}(\vec{q},\lambda) = (NM_\kappa)^{-1/2}\epsilon_\alpha(\kappa;q,\lambda)\, e^{i\vec{q}\cdot\vec{R}(l)}\ . \qquad (4.6)$$

Here $\epsilon_\alpha(\kappa;q,\lambda)$ is the αth Cartesian component of the polarization vector of the κth type of ion in the $q\lambda$ normal mode. $\vec{R}(l)$ is the lattice vector, and N is the number of unit cells.

Equation (4.5) contains the quantities

$$N_{nm} \equiv \langle Q_n(\Gamma j)|\, v(q,\lambda)\rangle\langle v(q,\lambda)|\, Q_m(\Gamma j)\rangle\ . \qquad (4.7)$$

Their explicit forms follow (for convenience we omit a factor N^{-1} from all expressions):

T_{1u}:

$$N_{00} = [\epsilon_\alpha(+;q\lambda)]^2\ , \qquad (4.8a)$$

$$N_{11} = 2[\epsilon_\alpha(-;q\lambda)]^2\cos^2 q_\alpha a\ , \qquad (4.8b)$$

$$N_{22} = 2[\epsilon_\alpha(+;q\lambda)]^2\cos^2 2q_\alpha a\ , \qquad (4.8c)$$

$$N_{01} = N_{10} = \sqrt{2}\epsilon_\alpha(-;q\lambda)\,\epsilon_\alpha(+;q\lambda)\cos q_\alpha a\ , \qquad (4.8d)$$

$$N_{02}=N_{20}=\sqrt{2}\,[\epsilon_\alpha(+;q\lambda)]^2\cos 2q_\alpha a\,, \tag{4.8e}$$

$$N_{12}=N_{21}=2\epsilon_\alpha(-;q\lambda)\,\epsilon_\alpha(+;q\lambda)(\cos q_\alpha)\cos 2q_\alpha a\,; \tag{4.8f}$$

A_{1g}:

$$N_{11}=\tfrac{2}{3}\,[\textstyle\sum_\alpha \epsilon_\alpha(-;q\lambda)\sin q_\alpha a]^2\,, \tag{4.9a}$$

$$N_{22}=\tfrac{2}{3}\,[\textstyle\sum_\alpha \epsilon_\alpha(+;q\lambda)\sin 2q_\alpha a]^2\,, \tag{4.9b}$$

$$N_{12}=N_{21}=\tfrac{2}{3}\,[\textstyle\sum_\alpha \epsilon_\alpha(-;q\lambda)\sin q_\alpha a]\times[\textstyle\sum_\beta \epsilon_\beta(+;q\lambda)\sin 2q_\beta a]\,; \tag{4.9c}$$

E_g:

$$N_{11}=[\epsilon_y(-;q\lambda)\sin q_y a-\epsilon_z(-;q\lambda)\sin q_z a]^2\,, \tag{4.10a}$$

$$N_{22}=[\epsilon_y(+;q\lambda)\sin 2q_y a-\epsilon_z(+;q\lambda)\sin 2q_z a]^2\,, \tag{4.10b}$$

$$N_{12}=N_{21}=[\epsilon_y(+;q\lambda)\sin 2q_y a-\epsilon_z(+;q\lambda)\sin 2q_z a]\times[\epsilon_y(-;q\lambda)\sin q_y a-\epsilon_z(-;q\lambda)\sin q_z a]\,; \tag{4.10c}$$

T_{2g}:

$$N_{11}=[\epsilon_x(-;q\lambda)\sin q_y a+\epsilon_y(-;q\lambda)\sin q_x a]^2\,, \tag{4.11a}$$

$$N_{22}=[\epsilon_x(+;q\lambda)\sin 2q_y a+\epsilon_y(+;q\lambda)\sin 2q_x a]^2\,, \tag{4.11b}$$

$$N_{12}=N_{21}=[\epsilon_x(-;q\lambda)\sin q_y a+\epsilon_y(-;q\lambda)\sin q_x a]\times[\epsilon_x(+;q\lambda)\sin 2q_y a+\epsilon_y(+;q\lambda)\sin 2q_x a]\,. \tag{4.11c}$$

We note here the following sum rule or normalization condition on $\mathrm{Im}G^0$ which is useful for our numerical normalization procedure: Integrating Eq. (4.5) over ω^2 leads to

$$\int \mathrm{Im}G^0_{nm}(\omega^2,\Gamma)\,d\omega^2=\pi\delta_{nm} \tag{4.12}$$

for each representation.

Once the defect matrix and unperturbed Green's-function matrix are known, we can write the perturbed Green's-function matrix G and the t matrix T as[10]

$$G=G^0(1+\Delta G^0)^{-1}=G^0\,L\,, \tag{4.13}$$

$$T=(1+\Delta G^0)^{-1}\,\Delta=L\Delta. \tag{4.14}$$

We now make the assumption that led to Eq. (2.5), namely, that only the first-neighbor ($n=1$) polarizability derivatives are nonzero. Then the Raman cross section will be proportional to

$$\pi\rho_{11}/2\omega=\mathrm{Im}G_{11}\,.$$

It is a property of the L matrix defined in Eq. (4.13) that G_{11} involves elements of G^0 and L in the defect space only:

$$G_{11}=G^0_{11}\,L_{11}+G^0_{12}\,L_{21}\,. \tag{4.15}$$

From Eq. (4.14) we see that the t matrix (required for infrared absorption) is also nonzero within the defect space. The matrix inversions to obtain L are carried out by the computer using complex arithmetic, and finally the imaginary parts of G_{11} and t are obtained. A brief description of the computer procedure is given in Sec. IV B.

B. Shell Model and Interpolation Schemes

The sodium chloride shell-model parameters used in our calculations were obtained by MacPherson[9] from a fit to the neutron-determined dispersion curves measured at a temperature of 80 K by Raunio, Almqvist, and Stedman.[8] The shell-model parameters are given in Table IV.

The Raman spectra in Figs. 1–4 are sufficiently detailed that a comparison with calculated curves of the previous type[5] would not afford a true test of the theoretical models. These previous calculations used 64 000 points in the first Brillouin zone. This led to constraints on histogram bin width not compatible with present experimental accuracy. A "point-to-point" calculation of $G^0(\omega^2,\Gamma)$ to achieve the required accuracy seems a waste of computer time. This difficulty prompted us to use two different interpolation schemes to calculate $G^0(\omega^2,\Gamma)$: a combined linear and quadratic (CLQ) scheme recently described by Cooke and Wood,[23] and the well-known Gilat–Raubenheimer (GR) scheme.[24] Our experience thus far has been that CLQ is 2–3 times faster but less accurate than GR—less accurate because it gives spurious singularities associated with crossing of dispersion curves. In the preliminary calculations we used the CLQ scheme, but in the final calculations reported here we have evaluated the inner products for different symmetries [cf. Eq. (4.6)] and the eigenfrequencies of host phonons for 2030 points in $\frac{1}{48}$ of the Brillouin zone (BZ) and have used the GR interpolation procedure. A typical histogram bin width

TABLE IV. Shell-model parameters: NaCl.

Parameter	Value	Unit
A	9.459	$e^2/2v$
B	−0.879	$e^2/2v$
B''	0.0438	$e^2/2v$
$B+B''$	−0.8352	$e^2/2v$
A_{++}	0.0	$e^2/2v$
B_{++}	0.0	$e^2/2v$
A_{--}	0.6272	$e^2/2v$
B_{--}	0.0084	$e^2/2v$
Z	0.8601	e
α_+	0.0035	v
d_+	0.0056	e
α_-	0.0495	v
d_-	0.1262	e
r_0	2.794	Å
U	43.6	Å^3
M_+	22.990	amu
M_-	35.475	amu

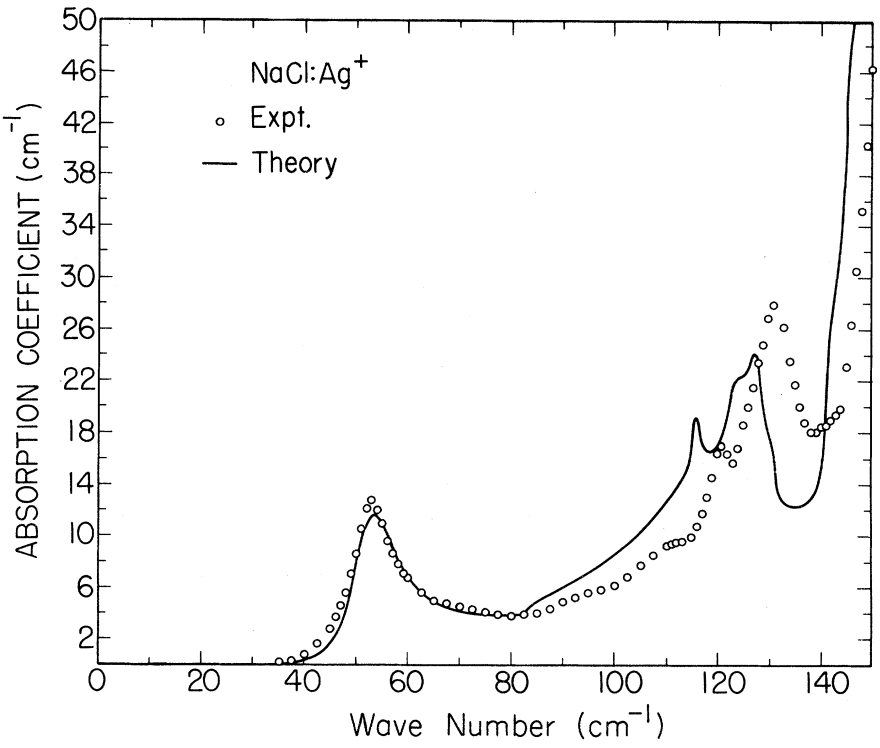

FIG. 6. The calculated ir absorption in NaCl : Ag^+ compared with 7 K experimental data from Ref. 4. The experimental data are represented by open circles. Impurity concentration N_I is 1.41×10^{20} cm^{-3}.

in the present calculation is about 0.02×10^{12} cps($\simeq 0.6$ cm^{-1}) which is about one-fourth the experimental resolution. A still narrower histogram bin width would be quite compatible with the accuracy of the interpolation scheme and could be used for interpreting fine structure in future Raman and ir work.

V. RESULTS OF CALCULATIONS AND DISCUSSION

A. Infrared Spectrum

The absolute quantitative result of the far-ir-absorption calculation using Eq. (2.1) with $n_\infty = 1.53$ and $e^* = 0.83e$ is compared with the old 7-K experimental data[16,4] for NaCl : Ag^+ in Fig. 6. The position, intensity, and shape of the 53-cm^{-1} peak are in excellent agreement with the calculation for $\Delta F_1 = -5000$ dyn/cm and $\Delta F_4 = -1000$ dyn/cm. The discrepancies in the positions of 120.5- and 131-cm^{-1} experimental peaks and their theoretical counterparts can probably be attributed to the use of shell-model parameters which fail to reproduce precisely the experimental host-crystal phonon frequencies in this frequency region.

For example, the 120.5-cm^{-1} experimental ir peak in Fig. 6 appears at 115 cm^{-1} in the calculated curve. A possible assignment of this peak is to the doubly degenerate phonon mode (W_3) at the point $W(1, 0.5, 0)$ in the BZ. Group theory predicts that W_3 will produce a T_{1u} defect-activated spectrum.[25] The neutron data give a value 120 cm^{-1} for this phonon frequency, whereas the shell-model parameters give a calculated frequency of 115 cm^{-1}. On the other hand, the experimental peak at 131 cm^{-1} in Fig. 6 does not appear to be associated with any phonons at high-symmetry points in k space.

B. Raman Spectra

In Figs. 7–9 we compare our theoretical calculations with experimental data for Raman scattering from NaCl : Ag^+ at 7 K for T_{2g}, E_g, and A_{1g} modes. The vertical scales are adjusted arbitrarily for a good fit. With our assumptions that the $\partial\alpha/\partial Q$'s are independent of ω and that only the 1nn ions have nonzero $\partial\alpha/\partial Q$'s, the low-temperature Raman cross section is directly proportional to $\mathrm{Im}G_{11}(\omega^2, \Gamma)$. The force-constant changes required to fit the experimental A_{1g}, E_g, and T_{2g} Raman spectra, along with those used for the T_{1u} mode ir calculation, are given in Table V. The present calculation accounts for most of the peaks observed experimentally. A broad peak at about 95 cm^{-1} in

TABLE V. Force-constant changes (in dyn/cm) used for calculated spectra.

Symmetry	ΔF_1	ΔF_4
T_{1u}	−5000	−1000
A_{1g}	+5900	0
E_g	−7500	−1600
T_{2g}	+750	0

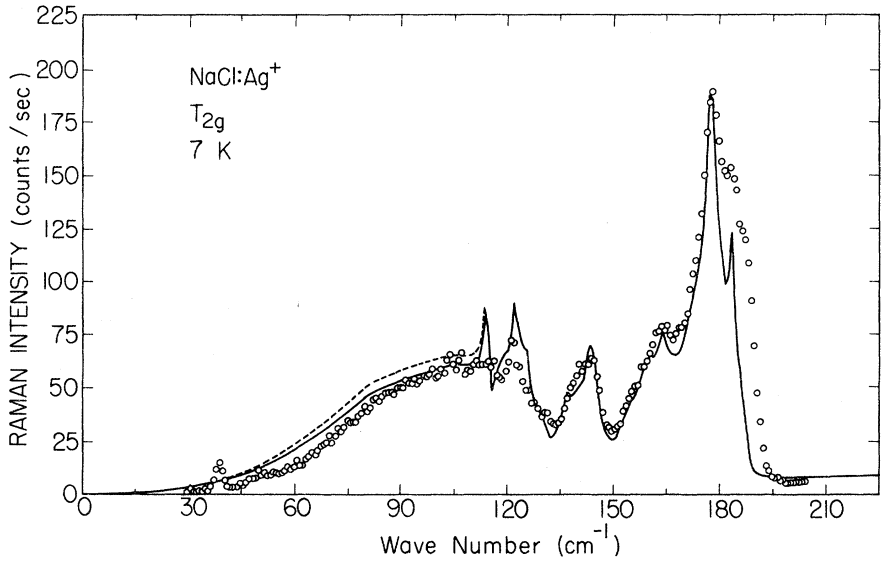

FIG. 7. Comparison of theoretical calculation with experimental data for Raman scattering from NaCl: Ag^+ at 7 K for the T_{2g} mode. Solid line: $\Delta F_1 = +750$ dyn/cm, dashed line: $\Delta F_1 = 0$.

the A_{1g} spectrum is probably due to E_g leakage and stray light as discussed in Sec. III B. The peaks at the low-energy part of the spectrum (~ 37 and 59.5 cm^{-1} in E_g, and ~ 137 cm^{-1} in T_{2g} spectra) cannot be found in our calculations. These peaks may be due to the pairing of the silver ions with other impurities. The only known Raman line due to pairs of Ag^+ ions is at 47 cm^{-1} and is found only in crystals where the Ag^+ concentration is greater than 1 mole%.[2] We did not observe it in our 0.5% crystal.

A summary of the experimental-and theoretical-peak positions for Raman (and far-ir) spectra is given in Table VI. From the table and from Figs. 7–9 one can see that most of the calculated peaks and other "critical points" (defined as places where the derivative of the spectrum is singular) have the correct qualitative shape and approximately the correct position. It is difficult to assign most of the critical points to specific regions of wave-vector space for the phonons. An exception may involve the relatively strong experimental peaks at 142 cm^{-1} found for all three Raman symmetries. We suggest that the peaks of A_{1g} and E_g symmetry might be due to W_1 phonons,[25] which occur at 140.5 cm^{-1} according to the neutron data.[8] There seems to be no analogous 140–144-cm^{-1} phonon at a high-symmetry point giving T_{2g} defect-activated spectra.

Apart from the critical points, the over-all shapes and relative intensities of the various parts of the spectra have to be considered. The ob-

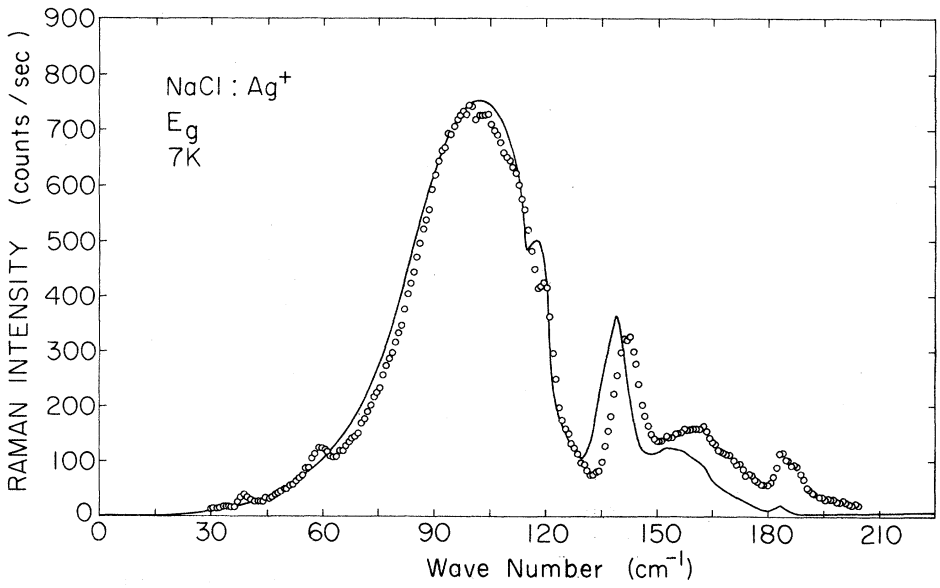

FIG. 8. Comparison of theoretical calculation with experimental data for Raman scattering from NaCl : Ag^+ at 7 K for the E_g mode.

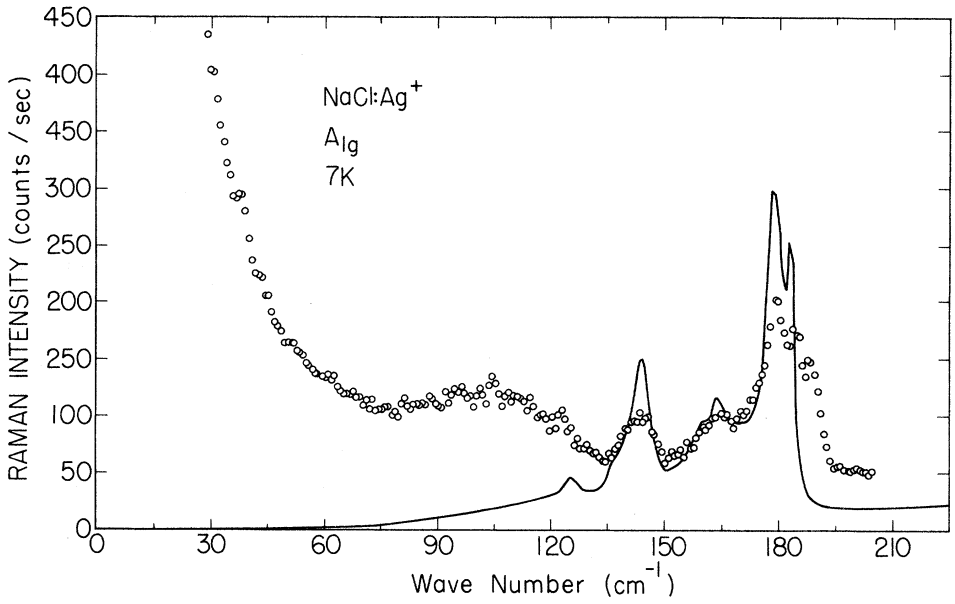

FIG. 9. Comparison of theoretical calculation with experimental data for Raman scattering from NaCl: Ag^+ at 7 K for the A_{1g} mode.

served T_{2g} spectrum is in quite good agreement with the calculated unperturbed $\mathrm{Im}G^0_{11}(\omega^2, T_{2g})$. This implies very little change in the noncentral force constant between the impurity and its nearest neighbors. The E_g spectrum requires a decrease in central force constants in order to explain the strong experimental peak at 96 cm^{-1}, a feature not found in the calculated unperturbed theoretical E_g curve shown in Fig. 10. An examination of the real parts of the E_g Green's functions and the condition for a resonance[10] shows that this peak is an "incipient resonance mode," similar to those found for the infrared sidebands of the U center in KBr and KI.[21,26] This strong perturbation of the E_g spectrum is quite different from that found for Tl^+ in potassium halides[13]; in that case practically no force-constant changes were necessary to fit the experimental E_g (and T_{2g}) spectra.

The A_{1g} spectrum apparently requires an increase in the central force constant. A comparison of the theoretical A_{1g} curves of Figs. 9 and 10 shows that the main result of this increase is to add more strength to the curve in the vicinity of 180 cm^{-1}. There were problems associated with the determination of the proper experimental background level, or base line, and with the subtraction of the T_{2g} spectrum from the raw data to obtain the A_{1g} spectrum. These make a determination of a "best fit" much more difficult for this spectrum than for the others. It appears that decreases in force constants are inconsistent with the A_{1g} data, and a moderate increase in force constant seems most likely.

C. Problems with High-Frequency E_g Spectrum

We do not understand the consistent mismatch of experimental and theoretical intensities in the high-energy part (135–180 cm^{-1}) of the E_g spec-

TABLE VI. Experimental and theoretical peak positions (in cm^{-1}) for far ir and Raman spectra for NaCl : Ag^+. The symbol s refers to shoulders in the spectra.

Expt E_g		Theory	Expt T_{2g}		Theory	Expt A_{1g}		Theory	Expt	Theory
7 K	78 K	E_g	7 K	78 K	T_{2g}	7 K	78 K	A_{1g}	T_{1u}(7 K)	T_{1u}
59.4	59.5		104.8	104.7		104.8	103.3		53.0	53.0
99.5	95.0		113.0	114.5	113.2	122.4	119.1	126.3		82.1 s
103.5	103.5	102.0	121.5	122.5	120.9	143.0	137.5–141.5	144.5	120.5	115.5
111.5 s	110.5–112.5 s		130.8	132.2	135.9	164.7	162.2	163.9		123.1 s
119.7	118.7	117.9	142.5	142.5	142.5	179.2	176.0	178.9	131.0	126.5
142.0	141.3	138.5	156.0 s	157.3 s	159.3	183.8	182.4	183.2		142.4 s
159.0	160.9	156.4	163.8	163.0	162.9	188.0	185.8		155.0	
183.0	183.7	183.3	178.5	178.7	176.0					
187.5	186.4		183.7	183.5	182.6					
			187.0 s	186.9	185.0					

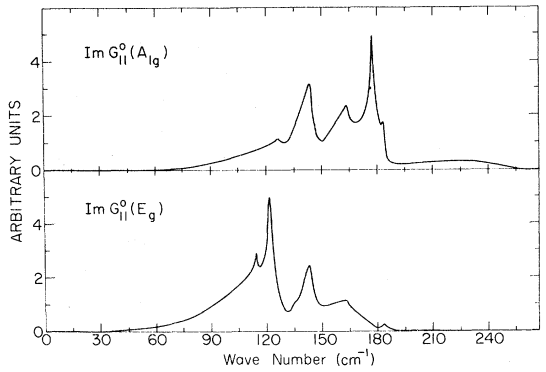

FIG. 10. Unperturbed A_{1g} and E_g Green's functions for host-crystal phonons in NaCl. Each curve is in separate arbitrary units.

trum; the contrast with excellent fit to the same part of the T_{2g} spectrum is striking. We have tried relaxing the assumption that only the 1nn ions have nonzero $\partial\alpha/\partial Q$'s. Suppose that the fourth neighbors have $\partial\alpha/\partial Q_2 \neq 0$. We see from Eq. (2.3) that the Raman cross section is then proportional to

$$\mathrm{Im}G_{11} + 2r\,\mathrm{Im}G_{12} + r^2\,\mathrm{Im}G_{22}\,, \tag{5.1}$$

where

$$r = \frac{\partial\alpha}{\partial Q_2} \Big/ \frac{\partial\alpha}{\partial Q_1}\,. \tag{5.2}$$

We found that for $r \simeq -0.05$, Eq. (5.1) gave about a 40% improvement in the high-frequency part of the E_g spectrum. For r in the range -0.2 to -0.3 this improvement was spoiled by a narrowing of the 96-cm^{-1} E_g incipient resonance peak and a shift of it to higher frequency. The corresponding changes in the A_{1g} spectrum were not significant.

It is worth noting in connection with this problem of the high-frequency E_g peaks that the unperturbed $\mathrm{Im}G^0_{11}$ shown in Fig. 10 fits them better than does the perturbed $\mathrm{Im}G_{11}$ shown in Fig. 8. Of course $\mathrm{Im}G^0_{11}$ does not give the 96-cm^{-1} E_g resonance.

D. Symmetry-Dependent Force-Constant Changes

Finally, we shall make a few comments on the symmetry dependence of the force-constant changes, which we found to be essential for the interpretation of the observed Raman spectra. A general justification for this result was given in Sec. IV. We now show that it follows quite straightforwardly from the assumptions of the relaxation model when changes of the bare Coulomb force constants among nearest neighbors are taken into account.[21]

To illustrate this, consider a simplified defect space consisting of the displacements of the impurity and its six 1nn ions. The force-constant change in this case [Eq. (4.3)] will be given by

$$\Delta_{11}(\Gamma j) = [K_{11}(\Gamma j) - K^0_{11}(\Gamma j)]\,, \tag{5.3}$$

with

$$K_{11}(\Gamma j) = \left(\frac{\partial^2 U}{\partial Q_1^2(\Gamma j)}\right)_0\,. \tag{5.4}$$

It is instructive to separate the potential energy U into Coulomb and repulsive parts and to consider separately the two contributions to the force-constant changes. We shall first show that for the perfect host crystal the Coulomb part of the force constant is symmetry dependent. A calculation,[27] based on Born–Mayer potentials, of the repulsive force constant per ion for either an A_{1g} or an E_g displacement of the Cl^- neighbors of a Na^+ ion in the perfect crystal gives $\Phi^0_{sr}(\Gamma) \simeq 41\,000$ dyn/cm. The calculation assumes that there is no deformation of the Cl^- ions and no second-neighbor Cl^--Cl^- repulsive interaction. A corresponding calculation using shell-model parameters gives

$$\Phi^0_{sr}(\Gamma) = 2(A + 2B) \simeq 40\,676 \text{ dyn/cm}.$$

A total-effective force constant for symmetry (A_{1g} or E_g) can be calculated from the zero-frequency Green's function[28] which yields the equation

$$\Phi^0_{eff}(\Gamma) = M_1[\mathrm{Re}G^0_{11}(0, \Gamma)]^{-1}\,. \tag{5.5}$$

A very approximate check on this calculation is provided by the equations

$$\Phi^0_{eff}(A_{1g}) \simeq 4r_0(C_{11} + 2C_{12})\,, \tag{5.6a}$$

$$\Phi^0_{eff}(E_g) \simeq 4r_0(C_{11} - C_{12})\,. \tag{5.6b}$$

These approximate expressions[28] can be evaluated from published data for the elastic constants C_{11} and C_{12}[29] and the lattice constant $2r_0$. The calculated values of $\Phi^0_{sr}(\Gamma)$ and $\Phi^0_{eff}(\Gamma)$ and their differences are given in Table VII. The differences between the A_{1g} and E_g values are quite large and strongly suggest the importance of the symmetry

TABLE VII. Effective (Φ^0_{eff}) and short-range (Φ^0_{sr}) part of the force constants for NaCl calculated from different considerations described in the text. The units are dyn/cm.

Symmetry	$\Phi^0_{eff}(\Gamma)$ From Green's functions	$\Phi^0_{eff}(\Gamma)$ From C_{ij}	$\Phi^0_{sr}(\Gamma)$ From first principles	$\Delta\Phi^0 = \Phi^0_{eff} - \Phi^0_{sr}$
A_{1g}	46 216.8	44 586.7	41 521.0	+4 695.8
E_g	28 866.4	25 760.5	40 799.0	−11 932.6

dependence of the Coulomb contribution, which is present in Φ^0_{eff} but not in Φ^0_{sr}.

We next consider the role of Coulomb interactions in determining force-constant *changes*. We work with the rigid-ion model and assume that the impurity has the same charge as the ion it replaces. The Madelung potential in the crystal is therefore unaltered, and since it varies as the fourth power of small displacements, its change can be neglected when any single ion is displaced. However, in a symmetrized displacement several ions are involved, and it is the change in the mutual Coulomb interaction of these ions alone which is the principal reason for the symmetry dependence of the force constants. It is easily shown that the changes in Coulomb energy for small displacements u of the 1nn ions from equilibrium are given approximately by

$$\delta U_c(A_{1g}) = (1+6\sqrt{2})\, e^2u^2/8r_e^3\,, \tag{5.7a}$$

$$\delta U_c(E_g) = -(3\sqrt{2}-1)\, e^2u^2/8r_e^3\,. \tag{5.7b}$$

r_e is the equilibrium distance from the defect site to the 1nn ions; in the perfect crystal $r_e = r_0$. Differentiating Eqs. (5.7a) and (5.7b) twice gives

$$\Phi_c(A_{1g}) = (1+6\sqrt{2})\, e^2/4r_e^3\,, \tag{5.8a}$$

$$\Phi_c(E_g) = -(3\sqrt{2}-1)\, e^2/4r_e^3\,. \tag{5.8b}$$

These equations alone are enough to show clearly that different force-constant changes for different modes are to be expected. The signs of $\Phi_c(A_{1g})$ and $\Phi_c(E_g)$ are such that an inward displacement of the 1nn ions ($r_e < r_0$) will qualitatively explain the signs of the force-constant changes which we have found necessary to fit the experimental data. To find quantitatively reliable estimates of force-constant changes would require fairly elaborate calculations, but they seem entirely feasible for certain types of substitutional impurities. Difficulties can be expected with T_{1u} modes where force-constant changes will be strongly influenced by the effects of ion polarization and deformation.[30,20,22] However, the importance of these effects for the T_{1u} modes again illustrates that different force constants for different modes are generally to be expected.

Note that for a system in which lattice relaxation around the impurity is small, contributions from Eqs. (5.7a) and (5.7b) are unimportant, and the dominant E_g and A_{1g} force-constant changes are given by the changes in the short-range repulsive part of the force constant, which are essentially symmetry independent. We thus suggest that the major part of the symmetry dependence of the A_{1g} and E_g force-constant changes is due to inward relaxation of the Cl^- neighbors and to a resulting symmetry dependence of the Coulomb part of the force-constant changes.

VI. CONCLUSIONS

Experimental defect-induced spectra of four symmetries A_{1g}, E_g, T_{2g} and T_{1u} have been compared with theoretical calculations. The position and nature of the observed critical points are explained quite well by the calculations, if one allows for some systematic errors in the calculated phonon frequencies. With the exception of the high-frequency E_g spectrum, which we do not yet fully understand, the broad features of the theoretical and experimental spectra are in quantitative agreement also. This agreement is obtained only by abandoning simple notions of symmetry-independent force-constant changes.

ACKNOWLEDGMENTS

We are grateful to T. Timusk and R. MacPherson for permission to use their unpublished shell-model parameters.

*Work was supported by the National Science Foundation under Contract Nos. GP 11173 and GP 28319, by the Advanced Research Projects Agency under Contract No. HC 15-67-C-0221, and by the U. S. Atomic Energy Commission under Contract with Union Carbide Corp.

†Present address: General Motors Corp., Research Laboratory, P.O. Box 388, Warren, Mich. 48089.

‡Present address and address during part of this work: Department of Physics and Materials Research Laboratory, University of Illinois, Urbana, Ill. 61801.

[1]R. Kaiser and W. Möller, Phys. Letters 28A, 619 (1969).

[2]W. Möller, R. Kaiser, and H. Bilz, Phys. Letters 31A, 309 (1970).

[3]W. Möller and R. Kaiser, Z. Naturforsch. 25a, 1024 (1970).

[4]H. F. Macdonald, M. V. Klein, and T. P. Martin, Phys. Rev. 177, 1292 (1969).

[5]R. F. Caldwell and M. V. Klein, Phys. Rev. 158, 851 (1967).

[6]R. Weber, Phys. Letters 12, 311 (1964).

[7]G. Benedek and G. F. Nardelli, J. Chem. Phys. 48, 5242 (1968).

[8]G. Raunio, L. Almqvist, and R. Stedman, Phys. Rev. 178, 1496 (1969).

[9]R. MacPherson, Ph.D. dissertation (McMaster University, Hamilton, Ontario, Canada, 1970) (unpublished).

[10]M. V. Klein, in *Physics of Color Centers*, edited by W. B. Fowler (Academic, New York, 1968), Chap. 7.

[11]Nguyen Xuan Xinh, A. A. Maradudin, and R. A. Coldwell-Horsfall, J. Phys. (Paris) 26, 717 (1965).

[12]G. Benedek and G. F. Nardelli, Phys. Rev. 154, 872 (1967).

[13]R. T. Harley, J. B. Page, and C. T. Walker, Phys. Rev. B 3, 1365 (1971).

[14]M. Born and K. Huang, *Dynamical Theory of Crys-*

tal Lattices (Oxford U. P., London, 1954), Chap. 4; G. P. Montgomery, Jr., Ph. D. dissertation (University of Illinois, Urbana, Illinois, 1971) (unpublished).
[15]R. Loudon, Advan. Phys. 13, 423 (1964); 14, 621 (E) (1965).
[16]H. F. Macdonald and M. V. Klein, in *Localized Excitations in Solids*, edited by R. F. Wallis (Plenum, New York, 1968), p. 46.
[17]R. L. Rosenbaum, Rev. Sci. Instr. 39, 890 (1968); 40, 577 (1969).
[18]J. G. Skinner and W. G. Nilsen, J. Opt. Soc. Am. 58, 113 (1968).
[19]Y. Kato and H. Takuma, J. Opt. Soc. Am. 61, 347 (1971).
[20]G. P. Montgomery, Jr., W. R. Fenner, M. V. Klein, and T. Timusk, Phys. Rev. B 5, 3343 (1972).
[21]T. Gethins, T. Timusk, and E. J. Woll, Phys. Rev. 157, 744 (1967).
[22]R. F. Wood and B. N. Ganguly (unpublished).
[23]J. F. Cooke and R. F. Wood, Phys. Rev. B 4, 1276 (1972).
[24]G. Gilat and L. J. Raubenheimer, Phys. Rev. 144, 390 (1966).
[25]R. Loudon, Proc. Phys. Soc. (London) 84, 379 (1964).
[26]T. Timusk and M. V. Klein, Phys. Rev. 141, 644 (1966).
[27]B. N. Ganguly and R. F. Wood (unpublished).
[28]G. Benedek and G. F. Nardelli, Phys. Rev. 167, 837 (1968).
[29]J. T. Lewis, A. Lehoczky, and C. V. Briscoe, Phys. Rev. 161, 877 (1967).
[30]H. Bilz, D. Strauch, and B. Fritz, J. Phys. (Paris) 27, Suppl. C2, 3 (1966).

PHYSICAL REVIEW B VOLUME 6, NUMBER 10 15 NOVEMBER 1972

Temperature Dependence of Luminescence of F^+ and F Centers in CaO†

B. Henderson
Solid State Division, Oak Ridge National Laboratory, Oak Ridge, Tennessee 37830
and Physics Department, Keele University, England

and

Y. Chen
Solid State Division, Oak Ridge National Laboratory, Oak Ridge, Tennessee 37830

and

W. A. Sibley
Solid State Division, Oak Ridge National Laboratory, Oak Ridge, Tennessee 37830
and Physics Department, Oklahoma State University, Stillwater, Oklahoma 74074

(Received 28 April 1972)

The principal moments of the F^+-center absorption and emission bands in CaO have been studied as a function of temperature in the range 5–300 K. The absorption results are shown to be in excellent agreement with the very recent results of Escribe and Hughes. Moment analysis is less useful for emission than absorption bands and gives no further information about the nature of the dynamic Jahn–Teller effect in the excited state of the F^+ center. Nevertheless, certain features of the temperature dependence of the first four moments of the broad band shape indicate that the Jahn–Teller interaction is still important even though the luminescence process samples the orbitally nondegenerate ground state. Analysis of the results shows that in the range 5–78 K the moments $M_1(0)$ and $M_2(T)$ can be accounted for with an effective Huang–Rhys factor $S=6$, the phonon modes effective in broadening the transition having a mean frequency $\hbar\omega = 273$ cm^{-1}. The first four moments of the $^3P \rightarrow {}^1S$ transition of the F center have been measured between 5 and 300 K. The results are interpreted as being consistent with $S=5.5$ and $\hbar\omega = 155$ cm^{-1}. Surprisingly, the band shape, as indicated by the ratio $R = M_4/(M_2)^2$, varies with temperature, being Gaussian below 90 K ($R=3.1$) and rather asymmetric with $R<3$ between 90–300 K. The experimentally measured line shapes in electron-irradiated crystals are well represented by Voigt profiles, which is interpreted as a convolution of the Gaussian component of the unirradiated crystal and that Lorentzian component due to point-defect broadening. The shape, shift, and broadening due to electron irradiation are qualitatively in agreement with the statistical theory of strain broadening.

I. INTRODUCTION

The optical properties of the irradiated and additively colored oxides have been investigated in considerable detail.[1–4] In particular, the F^+ center[2,3] in CaO has attracted considerable interest owing to the Jahn–Teller interaction in the first excited $^2T_{1u}$ state. Hughes[5] has shown that the experimental results are consistent with the idea that the Jahn–Teller coupling of the $^2T_{1u}$ state to the E_g and T_{2g} vibrational modes is equally strong and dominant over coupling to the A_{1g} breathing